PCCP

ROYAL SOCIETY OF CHEMISTRY

PAPER

View Article Online
View Journal



Cite this: DOI: 10.1039/d5cp03944d

# Investigating trends in actinide covalency and magnetism with $^{35/37}$Cl SSNMR spectroscopy and first-principles calculations

Adam R. Altenhof, †*[a] Karla A. Erickson, [b] Daniel A. Rehn, [c] Taylor V. Fetrow,[d] Ann E. Mattsson,[c] Marisa J. Monreal[e] and Harris E. Mason *[e]

Received 13th October 2025,
Accepted 30th March 2026

DOI: 10.1039/d5cp03944d

rsc.li/pccp

Solid-state NMR (SSNMR) spectroscopy is a powerful technique for studying actinide chemistry but has been significantly limited due to the complex paramagnetism, and radiological hazards presented by these materials. Lanthanide and actinide salts often feature magnetic ordering and can be paramagnetic, ferromagnetic, or antiferromagnetic depending on temperature and electronic structure. Paramagnetic interactions can manifest in SSNMR both as secular spectral shifts and/or couplings as well as contributions from non-secular relaxation. Both effects can be directly measured with NMR and used to extrapolate rich chemical information such as coordination environments, bonding characteristics, local molecular dynamics, and correlation times. Typically, these studies are carried out on high-$\gamma$ and highly abundant NMR-active isotopes (*e.g.*, $^{1}$H, $^{6/7}$Li, $^{19}$F, $^{23}$Na, *etc.*) or on enriched rare isotopes (*e.g.*, $^{2}$H and $^{17}$O), which can be expensive. Herein, we present a facile methodology to measure the $^{35/37}$Cl electric-field gradient (EFG) and paramagnetic shift anisotropy (SA) tensor components using static wideline SSNMR measurements of **$LaCl_3$**, **$NdCl_3$**, **$UCl_3$**, and **$UCl_4$**. The static powder spectra were measured with both $^{35}$Cl and $^{37}$Cl SSNMR to increase the fidelity of the extracted tensor parameters. Variable temperature NMR of a select case confirms the Curie–Weiss paramagnetism. Relaxation measurements of both nuclei further corroborate observations owing to the paramagnetic relaxation enhancement and reveal simultaneous quadrupolar relaxation mechanisms. Density functional theory (DFT) calculations using Hubbard *U* corrections to the uranium valence orbitals show excellent agreement with experimental EFG tensor parameters and help describe the bonding characteristics in these lanthanide and actinide systems.



## 1. Introduction

Actinide salts are a crucial component of molten-salt reactors (MSRs) where chloride salts are used as fuel sources for fissile isotopes (*e.g.*, $^{235}$U). The preparation of actinide chloride salts for MSRs currently lacks reliable and quantitative characterization techniques.[1–3] This limitation is largely due to (i) the hazards presented by radioactive actinide materials and (ii) the complicated physics of d and f electron orbitals involved in bonding that are reflected in available spectroscopies. The larger radial extent of d and f orbitals in actinides compared to the lanthanides has also been suggested to allow greater electron sharing with the valence electronic orbitals of ligands. Extensive studies combining X-ray based spectroscopies and *ab initio* modeling have explored these interactions, but direct modeling of these spectra is complex and open to interpretation.[4–8] NMR spectroscopy is one of the best available techniques for routine characterization and can provide information on local and longer-range structure and provides a direct measurement of the local electron density calculated by density functional theory (DFT). The measured NMR parameters are highly correlated to coordination environments and local bonding phenomena and can provide an insight to the complex valence systems of d and f orbitals in lanthanides and actinides.

Paramagnetic solid-state NMR (SSNMR) spectroscopy is a growing field that can provide rich information about coordination environments, bonding characteristics, and local molecular dynamics. Paramagnetism manifests in NMR due to the

[a] MPA-Q, Los Alamos National Laboratory, Los Alamos, NM 87545, USA. E-mail: adam.altenhof@eaps.ethz.ch
[b] C-CDE, Los Alamos National Laboratory, Los Alamos, NM, 87545, USA
[c] XCP-5, Los Alamos National Laboratory, Los Alamos, NM 87545, USA
[d] Sigma-1, Los Alamos National Laboratory, Los Alamos, NM 87545, USA
[e] C-IIAC, Los Alamos National Laboratory, Los Alamos, NM 87545, USA. E-mail: hmason@lanl.gov
† Current Address: Geothermal Energy and Geofluids Group, Department of Earth and Planetary Sciences, ETH Zürich, Zürich 8001, Switzerland.

coupling of unpaired electron spins to nuclear spins, referred to as the hyperfine coupling interaction as described by the hyperfine tensor, **A**, with the characteristic coupling constant, *A*. The interaction consists of an isotropic Fermi-contact component, $\mathbf{A}_{iso}$, which causes isotropic shifts in the resonance frequency of NMR spins, and a pseudo-contact anisotropic electron-nuclear spin dipolar coupling component, $\mathbf{A}_D$, which causes inhomogeneous broadening in these resonances. Both of these components can experience further inhomogeneous broadening when bulk magnetic susceptibility (BMS) effects are present.[9] The shifts and inhomogeneous broadening in the resulting NMR spectra can be quantified by the hyperfine tensor parameters, which are often summarized with shift anisotropy (SA) tensor parameters that reflect the sum of diamagnetic and paramagnetic contributions.[9–15] Pell *et al.* have provided a comprehensive overview of solution- and solid-state paramagnetic NMR spectra with many case studies.[16] Most of these studies are carried out with favorable NMR handles, *i.e.*, spin-1/2 and highly abundant nuclei, where studies with quadrupolar (spin $>$ 1/2) NMR handles are less common by comparison. Furthermore, there are many SSNMR studies of lanthanide materials but only limited reports for actinide materials.[17–30] Part of the limitation in the actinide studies is the hazard presented by radioactivity.[31]

Over the past 20 years there has been an increasing interest in the use of NMR-active quadrupolar halogens as SSNMR handles (*i.e.*, $^{35/37}$Cl, $^{79/81}$Br, and $^{127}$I). They are extremely sensitive to local structural changes and dynamics, as reflected in their measured electric-field gradient (EFG) tensor parameters. Of these handles, $^{35}$Cl is by far the most accessible for SSNMR studies. Although it has a low gyromagnetic ratio, it has a high natural abundance (75.78%) and a significantly smaller quadrupole moment, *Q*, than $^{79/81}$Br or $^{127}$I, causing the powder spectra to span reasonable breadths at high magnetic field strengths. $^{35/37}$Cl SSNMR studies have been carried out on a plethora of organic and inorganic materials as highlighted in several review articles by Bryce and coworkers.[32–35] Methodologies for studying $^{35/37}$Cl and similar NMR handles are continuing to improve with advances in static wideline and ultra-wideline NMR,[36–44] fast-MAS and indirect-detection techniques,[45,46] multiple-quantum approaches under MAS,[47–49] among others.[50] There have been previous $^{35}$Cl SSNMR studies of single crystal metal chloride salts with reported EFG and hyperfine tensor parameters, where the metals include paramagnetic $Ni^{2+}$, $Cu^{2+}$, $Mn^{2+}$, $Co^{2+}$, and $Fe^{2+}$ (depending on temperature).[51–55] However, there have been comparatively few reports of $^{35}$Cl SSNMR of crystalline powder materials that are paramagnetic,[56–58] with the exception of numerous perchlorate and chlorate samples.[33] Bauder and Wu recently reported $^{35/37}$Cl SSNMR of paramagnetic $Co^{2+}$ chlorides and demonstrated substantial shifts observed in $^{35/37}$Cl spectra.[59] Recently there have also been nuclear quadrupole resonance (NQR) studies of uranium complexes using $^{85/87}$Rb and $^{35}$Cl as spectroscopic handles, where only the influence of the EFG tensors can be measured in those cases.[60,61] There have been considerable efforts in the analysis of $^{2}$H SSNMR as simultaneously influenced by the first-order quadrupolar interaction (FOQI) and SA primarily using modified echo and Car-Purcell/Meiboom-Gill (CPMG) type pulse sequences.[62–69] The only comparable approaches of separating second-order quadrupolar interactions (SOQI) and SA interactions in half-integer spin nuclei are with the COASTER pulse sequence from Grandinetti *et al.*, which needs to be performed under MAS with a rotor angle of 70.12°,[70] and the TOP-STMAS/MQMAS method from Carvalho *et al.*, which also requires MAS.[71]

When studying half-integer-spin quadrupolar nuclei such as $^{35/37}$Cl ($I = 3/2$), researchers often focus on the acquisition of the central transition (CT) powder pattern, which spans a far narrower frequency breadth comparted to the satellite transitions (STs). CT powder patterns can be simultaneously influenced by the SOQI, SA interactions, and/or dipole–dipole interactions; herein, we focus on simultaneous SOQI and shielding interactions. The complicated orientation dependence of the SOQI convolved with the effects of SA results in static powder spectra that are difficult to analyze and deconvolve their individual contributions.[72] The problem in these cases is that eight parameters are needed to accurately model the EFG and SA tensor parameters (two for the EFG, three for the SA, and three Euler angles relating the orientations of the two tensors). To accurately determine all eight parameters, multiple NMR spectra are required. Typically, a pattern should be recorded under MAS, in which the manifestation of the SA parameters is averaged, and a static pattern should be measured. Then both should be acquired at a second magnetic field such that the manifestation of the EFG and SA parameters will change. One problem with this strategy is for cases where the inhomogeneous broadening (from EFG, SA, or both) is too large for sufficient averaging of under MAS, where complex spinning sideband manifolds can hamper analysis. Furthermore, access to a second magnetic field is not a ubiquitous option for researchers and in the current work, radioactive samples are measured where limited exposure to multiple pieces of equipment and spectrometers is desirable.

Instead, the use of $^{37}$Cl NMR as a compliment to $^{35}$Cl measurements can mimic the effects of measuring $^{35}$Cl at a second higher-magnetic field. A higher field will cause a decrease in pattern broadening from the SOQI (with a $\nu_Q^2/B_0$ dependence, where $\nu_Q$ is the quadrupolar frequency) and a linear increase in broadening from magnetic shielding (linear $B_0$ dependence). $^{37}$Cl will experience a smaller $C_Q$ as compared to $^{35}$Cl (as scaled by the ratio of their quadrupolar moments, $Q(^{37}Cl)/Q(^{35}Cl) = 0.78812$) and the same $\eta_Q$ resulting in less inhomogeneous broadening from the SOQI and will be influenced by nearly identical SA tensor parameters.[73–75] Using $^{35/37}$Cl together can provide a much simpler experimental strategy for determining multiple tensor parameters since the Larmor frequencies are close together (*i.e.*, a single broadband probe can measure both) and limit exposure for radioactive materials.

Herein, we discuss the use of $^{35/37}$Cl SSNMR to study lanthanide and actinide chloride salts. The central strategy for this study is to use static $^{35}$Cl SSNMR measurements to establish the EFG and paramagnetic SA tensor parameters and then confirm them with $^{37}$Cl SSNMR measurements. In every

 

case 1D spectra, $T_1$'s, and $T_2^{eff}$'s are measured and compared between the compounds studied. We also calculate local molecular orbitals (LMOs) and bond order parameters from periodic DFT calculations to help constrain the origins of the SA and EFG tensors to provide insight into the relative covalency of the metal–chloride bonds.

# 2. Methods

## 2.1. Samples

Lanthanum trichloride [Strem Chemicals Inc., **$LaCl_3$**] and neodymium trichloride [Strem Chemicals Inc, **$NdCl_3$**] were purchased. Depleted uranium trichloride [**$UCl_3$**][76] and uranium tetrachloride [**$UCl_4$**][2,3,77] were prepared according to literature procedures. Radioactive **$UCl_3$** and **$UCl_4$** samples were transferred into polychlorotrifluoroethylene (PCTFE) inserts within 4 mm zirconia NMR rotors and non-radioactive samples were packed directly into the rotor sleeves; therefore, measurements of radioactive samples contain less material. Sample purity was confirmed by powder Xray diffraction (XRD) patterns (see SI).

## 2.2. SSNMR Spectroscopy

SSNMR spectra were acquired using a Bruker Avance NEO console and a 9.4 T ($\upsilon_0(^1H)$ = 399.94 MHz) Bruker wide-bore magnet at resonance frequencies of $\upsilon_0(^{35}Cl)$ = 39.186 MHz and $\upsilon_0(^{37}Cl)$ = 32.618 MHz. Two Bruker broadband 4 mm HX magic-angle spinning (MAS) probes were used under static conditions, where one was used for radioactive samples and the other was used for non-radioactive samples to limit the potential for equipment contamination. $^{35/37}$Cl RF pulse powers and chemical-shift reference frequencies were calibrated using NaCl (s) with $\delta_{iso}$ = 0.0 ppm. All spectra were recorded with the WURST-CPMG pulse sequence with varied parameters (see SI).[36,37,78–80] The temperature reading for variable temperature (VT) experiments was calibrated using the $^{207}$Pb SSNMR of $PbNO_3$.[81] All other measurements were made under ambient conditions around 20 °C. $^{35/37}$Cl effective $T_2$'s ($T_2^{eff}$) were measured using the WURST-CPMG time-domain data and $T_1$'s were measured with a WURST-CPMG/Saturation-Recovery (WCPMG-SR) type pulse sequence using 16 relaxation delays.[82]

## 2.3. Processing and simulations

All data were processed with Python using DESPERATE and NMRGLUE.[83,84] WURST-CPMG echo trains were coadded into a single echo, multiplied by a Gaussian function, Fourier transformed, then phase corrected with zeroth, first, and second-order phasing[85] in every case. Subsequent simulations and fitting were conducted in ssNake version 1.3.[86] Additional SIMPSON simulations are presented in the SI.[87,88]

## 2.4. Density functional theory

Plane wave DFT calculations were carried out using the Vienna *Ab initio* Simulation Package (VASP) version 5.4.4.[89–92] The Revised Perdew–Burke–Ernzerhof (PBE) functional[93] with both the Hubbard $U$ correction (DFT+$U$) was used for calculations of the paramagnetic **$NdCl_3$**, **$UCl_3$**, and **$UCl_4$** materials. The rotationally invariant method of Dudarev *et al.* was used where $U_{eff} = U - J$,[94] where $J$ is the on-site exchange interaction and in all cases was set to 0 eV. These materials were calculated in the ferromagnetic state and scaled to the paramagnetic regime using a Curie–Weiss model as described in Kim *et al.*[95] The optimal $U_{eff}$ value was obtained by running calculations for different $U_{eff}$ values and determining the best match to the measured EFG tensors (Fig. S9–S12). Calculations were also performed including spin–orbit coupling but provided qualitatively inaccurate results for **$NdCl_3$** and had minor effects on those for **$UCl_3$** and **$UCl_4$** (Table S3). Thus, all calculations reported in the main text were performed in the absence of spin–orbit coupling for consistency. All calculations were performed on the unrelaxed XRD structures drawn from the literature. A plane-wave kinetic energy cutoff of 500 eV and convergence energy difference of $10^{-8}$ eV were used for EFG and chemical shift calculations. The local orbital basis suite towards electronic-structure reconstruction (LOBSTER) software package was used to perform crystal orbital Hamiltonian population (COHP), crystal bond order index (COBI), and reconstructed local molecular orbital (RLMO) analyses.[96–98] The bond-weighted values of the COHP and COBI are reported as the integrated crystal Hamiltonian population (ICOHP) and integrated crystal bond order index (ICOBI).

# 3. Results and discussion

## 3.1. Overview

In the following sections, $^{35}$Cl and $^{37}$Cl SSNMR measurements are conducted on **$LaCl_3$**, **$NdCl_3$**, **$UCl_3$**, and **$UCl_4$**, which all feature a single chlorine site. Diamagnetic **$LaCl_3$** is used as a control, since it is expected to exhibit CT powder spectra only influenced by the SOQI, which will serve to baseline the EFG tensor parameters for structurally similar analogues. All subsequent samples are paramagnetic at room temperature and are expected to be influenced by paramagnetic SA interactions. $^{35}$Cl spectra are used to establish both the EFG and SA parameters using fits in ssNake and $^{37}$Cl spectra are used to confirm the fitted parameters. Variable temperature (VT) $^{35}$Cl NMR is used to verify the paramagnetic SA parameters in a select case for **$NdCl_3$**. In every case the $^{35/37}$Cl $T_1$'s and $T_2^{eff}$'s are measured and compared. DFT calculations help constrain the fitted EFG and SA tensor parameters and provide insight to the type of bonding in these lanthanide and actinide chloride compounds.

## 3.2. $^{35/37}$Cl SSNMR

$^{35}$Cl SSNMR was conducted on all samples outlined above (Fig. 1). The first compound considered is **$LaCl_3$** (Fig. 1a), which features a single chlorine site that is in a 9-coordinate geometry around $La^{3+}$.[99] The static powder pattern is fit in ssNake where the EFG and SA tensor parameters are extracted. The fitted parameters for this and all compounds are summarized in Table 1, where **$LaCl_3$** has $C_Q$ = 7.91 MHz, $\eta_Q$ = 0.49, $\delta_{iso}$ = 302.3 ppm, and all other SA parameters are negligible. There is no discernable

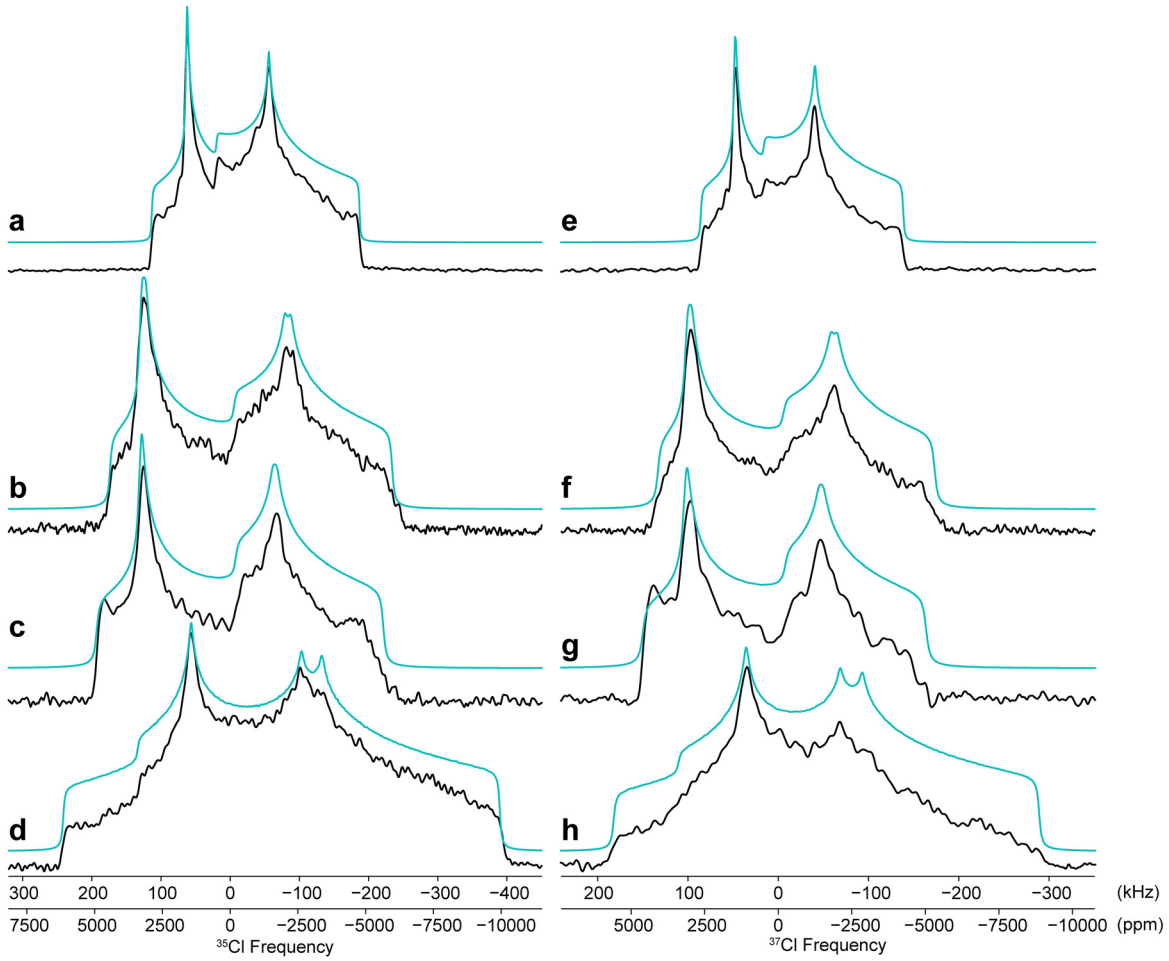


Fig. 1 $^{35}$Cl NMR spectra of (a) **$LaCl_3$**, (b) **$NdCl_3$**, (c) **$UCl_3$**, and (d) **$UCl_4$** and $^{37}$Cl NMR of the same compounds, respectively (e–h). Experimental spectra are in black and simulated fitted spectra generated in ssNake are in blue. Spectra are not plotted on the same relative intensity scale.

Table 1 Experimental and calculated $^{35/37}$Cl SSNMR EFG and SA tensor parameters[a,b,c] and calculated bonding parameters[d]

| Compound | | $U_{eff}$ (eV) | $C_Q$ ($^{35}$Cl) (MHz) | $\eta_Q$ | $\delta_{iso}$ (ppm) | $\Omega$ (ppm) | $\kappa$ (ppm) | $\alpha$ (°) | $\beta$ (°) | $\gamma$ (°) | ICOHP (eV) | ICOBI[d] |
|---|---|---|---|---|---|---|---|---|---|---|---|---|
| **$LaCl_3$** | Exp. | | 7.91 | 0.49 | 302.3 | 0 | 0.00 | 0.0 | 0.0 | 0.0 | | |
| | DFT | 4.0 | 7.87 | 0.53 | 731 | | | | | | −1.13 | 0.19 |
| **$NdCl_3$** | Exp. | | 8.99 | 0.48 | 758.5 | 2004 | 0.52 | 9.2 | 4.5 | 0.0 | | |
| | DFT | 1.0 | 8.98 | 0.49 | 1738 | 2549 | 1.00 | | | | −1.17 | 0.20 |
| **$UCl_3$** | Exp. | | 8.68 | 0.52 | 1014.0 | 2255 | 1.00 | 20.4 | 2.0 | 0.0 | | |
| | DFT | 6.0 | 9.25 | 0.58 | 1071 | 2038 | 0.99 | | | | −1.10 | 0.19 |
| **$UCl_4$** | Exp. | | 12.00 | 0.35 | 600.0 | 5200 | −0.01 | 0.0 | 8.5 | 0.0 | | |
| | DFT | 5.0 | −11.99 | 0.31 | −393 | 3283 | −0.43 | | | | −1.65 | 0.29 |

[a] The principal components of the EFG tensors are ranked $|V_{33}| \geq |V_{22}| \geq |V_{11}|$. The quadrupolar coupling constant and asymmetry parameter are given by $C_Q = eQV_{33}/h$, and $\eta_Q = (V_{11} - V_{22})/V_{33}$, respectively. The sign of $C_Q$ cannot be determined from the experimental $^{35/37}$Cl spectra. [b] The principal components of the SA tensors are defined such that $\delta_{11} \geq \delta_{22} \geq \delta_{33}$. The isotropic shift, span, and skew are given by $\delta_{iso} = (\delta_{11} + \delta_{22} + \delta_{33})/3$, $\Omega = \delta_{11} - \delta_{33}$, and $\kappa = 3(\delta_{22} - \delta_{iso})/\Omega$, respectively. Calculated SA parameters use the full **A** tensor according to Pigliapochi *et al.*[115] [c] The Euler angles $\alpha$, $\beta$, and $\gamma$ define the relative orientation of the EFG and SA tensors. Euler angles are reported using the $ZX'Z''$ convention.[129,130] [d] The ICOHP and ICOBI values represent bond-weighted averages.

influence of SA on the static powder pattern within the precision of our measurements. The $\delta_{iso}$ reported is well within the range of diamagnetic shielding that is often reported for $^{35}$Cl SSNMR of metal complexes and iconic compounds.[32–34] These tensor parameters and the visual appearance of the spectrum and its discontinuities are highly commensurate with a typical static SOQI CT powder pattern, which is consistent with the material being diamagnetic.

**$NdCl_3$** was then investigated, which is structurally similar to **$LaCl_3$** since both compounds occupy a $P6_3/m$ space group, are both 9-coordinate to the metal center, and have very similar M–Cl bond distances (2.95 and 2.97 Å for **$LaCl_3$**; 2.90 and 2.95 Å for **$NdCl_3$**).[99] The main difference is the unpaired 4f electrons of $Nd^{3+}$. The resulting $^{35}$Cl pattern (Fig. 1b) is significantly different from that of **$LaCl_3$** where similar EFG parameters are found with $C_Q$ = 8.99 MHz, $\eta_Q$ = 0.48, but significant SA parameters are necessary to fit the spectrum with $\delta_{iso}$ = 785.5 ppm, $\Omega$ = 2004 ppm, and $\kappa$ = 0.52. For comparison, the pattern was fitted without SA parameters, which causes a significant mismatch in the central discontinuity and the broadening of the ''horn'' features in the powder pattern (Fig. S5). This $\delta_{iso}$ and $\Omega$ are amongst the largest reported for $^{35}$Cl NMR and are unlikely to arise from diamagnetic shielding. Since **$NdCl_3$** is paramagnetic, it is very likely that the SA tensor parameters are primarily from the manifestation of paramagnetic shielding, especially as compared to the diamagnetic **$LaCl_3$**, which is almost identical in structure.

**$UCl_3$** is also structurally similar to **$LaCl_3$** and **$NdCl_3$** (*i.e.*, they have the same space group, coordination environment, and similar bond distances)[100] but like **$NdCl_3$**, $U^{3+}$ features unpaired f electrons (5f in this case) and is paramagnetic at room temperature. The $^{35}$Cl pattern of **$UCl_3$** (Fig. 1c) is visually much more similar to that of **$NdCl_3$** rather than **$LaCl_3$** and has similar EFG tensor parameters to both with $C_Q$ = 8.68 MHz and $\eta_Q$ = 0.52. The SA parameters are significantly larger than both **$LaCl_3$** and **$NdCl_3$** with $\delta_{iso}$ = 1014 ppm, $\Omega$ = 2255 ppm, and $\kappa$ = 1.00. **$UCl_3$** has a slightly higher paramagnetic susceptibility value than **$NdCl_3$**, which could be one source for the larger SA tensor components, and it is structurally very similar to **$NdCl_3$**, which is reflected in the EFG tensor parameters.

**$UCl_4$** is structurally unique from the trichloride compounds analyzed above, occupying an $I4_1/amd$ space group and having an 8-coordinate geometry around $U^{4+}$.[101] The $^{35}$Cl powder pattern (Fig. 1d) is substantially broader than the others, owing to both the EFG parameters of $C_Q$ = 12.0 MHz and $\eta_Q$ = 0.35 and the SA parameters with $\delta_{iso}$ = 600 ppm, $\Omega$ = 5200 ppm, and $\kappa$ = –0.01. The larger $C_Q$ and substantial $\Omega$ cause the large frequency dispersion in this case. The $\delta_{iso}$ is less than that of **$NdCl_3$** and **$UCl_3$**, but still much larger that of **$LaCl_3$**, which matches the relative magnetic susceptibility between all the compounds (*vide infra*).

As mentioned earlier, it is difficult to isolate the EFG and SA parameters simultaneously using only one spectrum at one field and only acquired under static conditions as there are eight free variables involved in the fit. The $^{35}$Cl powder patterns presented herein are far too broad to garner useful information from MAS experiments at moderate speeds and may still be difficult with ultrafast MAS (Fig. S6). The issue of using MAS would not be alleviated at separate magnetic fields, since the net pattern breadth will increase at lower fields, marginally decrease at some higher fields, and increase at significantly higher fields (Fig. S7). Static measurements at a second magnetic field would be a useful check and constraint on the parameters; however, our laboratory (like many others) is equipped with only a single SSNMR system, and even with a second system, additional equipment would be exposed to radiological hazards. Therefore, using the $^{37}$Cl isotope as a handle for a second reference for the tensor parameters is an ideal alternative for simplicity and safety. Any shift differences experienced by the nuclei should be far less than the precision of our measurements.[74]

The $^{37}$Cl NMR spectra were acquired for all the compounds described above (Fig. 1e–h). In every case, the tensor parameters from the fits of the $^{35}$Cl data were used to simulate the $^{37}$Cl spectra (expect for the $C_Q$, which was scaled accordingly). In each case, the simulated spectra match the experimental well. The main drawbacks of $^{37}$Cl are the slightly lower gyromagnetic ratio and its natural abundance being about one third of $^{35}$Cl causing a lower receptivity; therefore, the experimental $^{37}$Cl are slightly lower in signal-to-noise ratios and in some cases require slightly more Gaussian broadening. Nonetheless, the main discontinuities between all spectra align well, with the exception of the **$UCl_4$** pattern (Fig. 1h). This pattern appears to experience a bandpass-type depletion of signal, especially to the low-frequency part of the pattern, making it harder to clearly resolve the lower frequency horn (and its splitting) as well as the low frequency pattern edge, but is still discernable. There is also an anomalous feature in both $^{35/37}$Cl patterns of **$UCl_3$** where the high-frequency edge shows a peak-like feature (Fig. 1c and g). This may be due to $T_1$ or $T_2$ anisotropy, which would require much more sensitive measurements to confirm.[82,102] It is important to note that $^{37}$Cl spectra are not used for fitting but serve as a check against the fitted parameters from the $^{35}$Cl data, increasing our confidence in both the EFG and SA tensor parameters across all compounds.

Having established that chloride compounds containing elements with non-negligible paramagnetic susceptibilities cause the onset of the effects of SA interactions, it is important to rule out that nuclear magnetic shielding (*i.e.*, diamagnetic shift or chemical shift) is causing these effects. The paramagnetic susceptibility and therefore the SA tensor parameters should exhibit a $1/(T - \Theta)$ temperature dependance, provided the temperature exceeds the Weiss constant, $\Theta$.[9,16] The VT $^{35}$Cl SSNMR experiments were carried out for **$NdCl_3$** since its lack of radioactivity allows us to measure more sample (due to our sample-packing technique).

The $^{35}$Cl SSNMR of **$NdCl_3$** was measured between *ca.* –10 °C and +50 °C (Fig. 2a). The $^{35}$Cl SSNMR spectra were recorded at each temperature using the same acquisition parameters as in Fig. 1b for the same amount of time (about 1 hour per spectrum). As the temperature increases, a noticeable shift in the high-frequency discontinuities of the $^{35}$Cl powder patterns are discernable (*i.e.*, the edge and ''horn'' discontinuities as marked with dashed lines). However, there is no shift observed in the lower-frequency discontinuities. If the EFG parameters were changing with temperature, which can happen in dynamical systems,[103–105] then both the high- and low-frequency features of the pattern would be expected to change (*i.e.*, if a larger or smaller effective $C_Q$ was observed due to motional averaging, then the entire breadth of the pattern should grow or

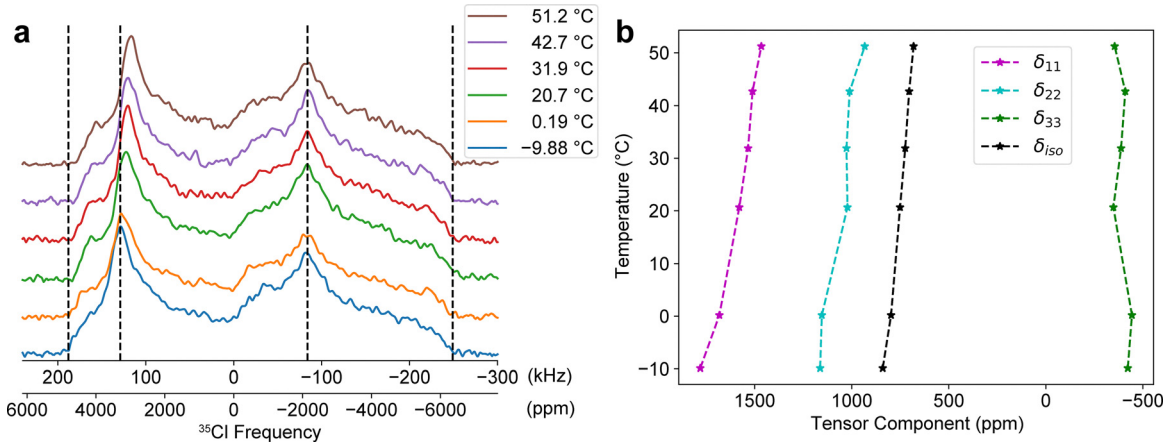


Fig. 2 (a) Experimental variable temperature (VT) $^{35}$Cl NMR spectra of **$NdCl_3$**. Vertical dashed lines are drawn to indicate discontinuities in the powder pattern acquired at −9.88 °C. (b) SA tensor components extracted from fitting each experimental spectrum and plotted in standard convention for visual clarity where $\delta_{iso} = (\delta_{11} + \delta_{22} + \delta_{33})/3$.

shrink, respectively – Fig. S8). Therefore, it is safe to conclude that only the SA tensor parameters could be changing in this case. The subsequent spectra were fit in ssNake using the established EFG tensor parameters from Fig. 1b and Table 1 as a starting point then the SA tensor parameters alone were fitted at each temperature. A summary of the fitted SA tensor parameters in standard convention are summarized in Fig. 2b. $\delta_{iso}$ is found to shift from 840.2 to 681.4 ppm over the temperature range. The fitted $\delta_{iso}$'s were fit with a linear function with $R^2 = 0.989$. Therefore, the $\delta_{iso}$ exhibits a $1/(T - \Theta)$ temperature dependence characteristic of the Curie–Weiss paramagnetic shielding. **$UCl_3$** is nearly identical in structure to **$NdCl_3$** and has a slightly higher paramagnetic susceptibility; therefore, it is safe to assume that **$UCl_3$** also experiences the Curie–Weiss paramagnetic shielding.

The relative $^{35/37}$Cl isotropic shift is compared across all samples (Fig. 3a). The shifts are plotted against the effective magnetic moment, $\mu_{eff}$, of each compound. The room temperature $\mu_{eff}$ is zero for **$LaCl_3$** and is known for **$UCl_3$** (3.70) and **$UCl_4$** (3.29),[106] but not for **$NdCl_3$**; therefore a $\mu_{eff}$ of 3.52 $\mu_B$ was measured at 298 K using a Gouy balance. The shifts generally increase with the $\mu_{eff}$'s where the hyperfine constant, $A \propto \mu_{eff}$. However, the origin of the shifts in each sample can vary greatly with the changing electronic structure and is considered further in DFT calculations (*vide infra*). This same $\mu_{eff}$ trend is not observed in $\Omega$, specifically with the large $\Omega$ = 5200 ppm for **$UCl_4$** (Table 1), which may suggest a significant dipolar contribution to the hyperfine coupling for this compound.

### 3.3. Relaxation measurements

Relaxation measurements were carried out for the $^{35/37}$Cl NMR data described above. The $T_1$ is measured for both nuclei using a saturation-recovery (SR) type pulse sequence with WURST-CPMG signal detection.[82,107] Inversion recovery experiments are more accurate in part due to the higher variation in range, but SR offers significantly faster measurements.[108,109] Since every 1D spectrum in this work is measured with the

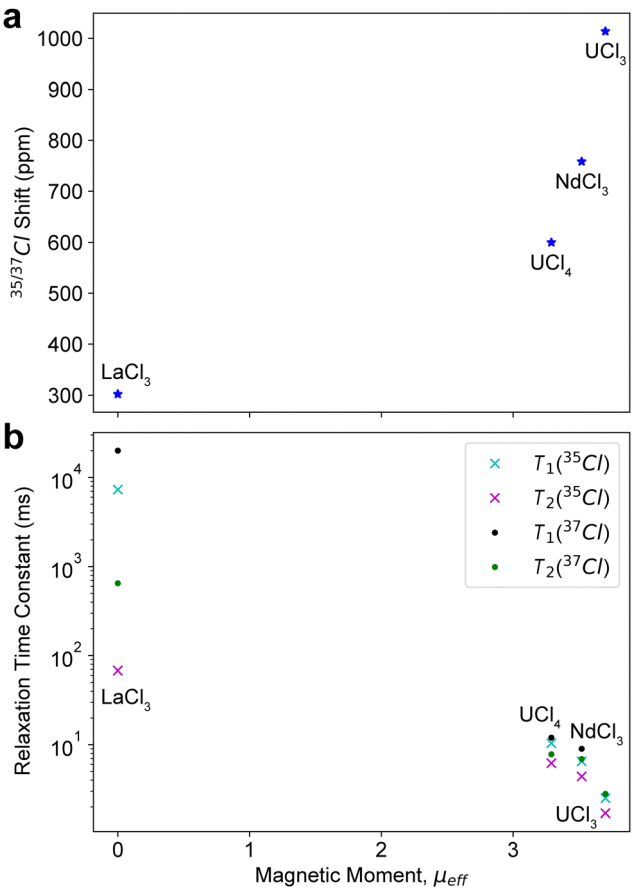


Fig. 3 (a) $^{35/37}$Cl $\delta_{iso}$'s and (b) $^{35/37}$Cl relaxation constants plotted as a function of the effective magnetic moment of each compound studied. $\mu_{eff}$ = 0.00, 3.29, 3.52, 3.70 for **$LaCl_3$**, **$UCl_4$**, **$NdCl_3$**, and **$UCl_3$** respectively.

WURST-CPMG pulse sequence, the effective-$T_2$, $T_2^{eff}$, is obtained by default in every case, which also aids in signal detection by increasing the signal-to-noise of the spectra. It is important to note that multiple aspects of CPMG acquisition affect the

Table 2 $^{35/37}$Cl NMR relaxation constants

| Compound | $T_1$ ($^{35}$Cl) (ms) | $T_1$ ($^{37}$Cl) (ms) | $T_2^{eff}$ ($^{35}$Cl)[a] (ms) | $T_2^{eff}$ ($^{37}$Cl)[a] (ms) |
|---|---|---|---|---|
| **$LaCl_3$** | $(7.3 \pm 0.2) \times 10^3$ | $(20 \pm 2) \times 10^3$ | $68 \pm 5$ | $650 \pm 10$ |
| **$NdCl_3$** | $6.5 \pm 0.3$ | $9.0 \pm 0.5$ | $4.4 \pm 0.1$ | $6.9 \pm 0.3$ |
| **$UCl_3$** | $2.5 \pm 0.4$ | $2.8 \pm 0.3$ | $2.3 \pm 0.3$ | $2.8 \pm 0.2$ |
| **$UCl_4$** | $10.4 \pm 0.9$ | $12 \pm 0.1$ | $6.2 \pm 0.1$ | $7.8 \pm 0.2$ |

[a] $T_2^{eff}$'s are measured with varying echo delays, RF amplitudes, and WURST sweepwidths (see SI).

measured $T_2^{eff}$ and this is not necessarily a reliable metric when ascribing physical differences between measurements and samples. Many experimental WURST-CPMG or standard (Q)CPMG parameters will impact the measured $T_2^{eff}$ including the echo delay times, RF fields, pulse widths, flip angles, pulse phase, and the accumulated errors in refocusing pulses.[41,110–114] $T_1$'s are not susceptible to these aforementioned effects and should be considered a far more reliable relaxation measurement, but since the $T_2^{eff}$ is measured by default herein, it is also analyzed.

The measured $^{35/37}$Cl relaxation constants are summarized in Table 2 and Fig. 3b. As mentioned above, **$LaCl_3$** is diamagnetic and features no influence from SA and has $T_1(^{35}Cl) = 7.3 \pm 0.2$ s. This is compared to **$NdCl_3$** with $T_1(^{35}Cl) = 6.5 \pm 0.3$ ms, which is approximately three-orders of magnitude smaller than **$LaCl_3$**. Based on the 1D NMR spectra across all the compounds, the only contributing NMR interactions are the quadrupolar and SA interactions; therefore, these are also likely the only contributors to the non-secular relaxation. If quadrupolar relaxation was dominant, such a dramatic decrease in $T_1(^{35}Cl)$ would not be expected for the $C_Q$ only differing by about 1 MHz between samples (*i.e.*, for quadrupolar relaxation, $1/T_1 = R_1 \propto {C_Q}^2$). Therefore, the $T_1(^{35}Cl)$ difference between the two samples is likely characteristic of the paramagnetic relaxation enhancement (PRE), which has $R_1 \propto A^2 \propto {\mu_{eff}}^2$. **$UCl_3$** and **$UCl_4$** likewise feature $T_1(^{35}Cl)$ values that are *ca.* 1000-fold smaller than **$LaCl_3$**. The $T_1(^{35}Cl)$ differences between **$NdCl_3$**, **$UCl_3$**, and **$UCl_4$** all correlate well with their $\mu_{eff}$'s (Fig. 3b) commensurate with PRE. Although not as reliable as the $T_1$ measurements, the same relaxation trends across these samples are also observed in the $T_2^{eff}(^{35}Cl)$ values. The difference between the $T_2^{eff}(^{35}Cl)$ of **$LaCl_3$** and the other samples is not as stark as the $T_1(^{35}Cl)$'s, likely because of the added secular factors impacting $T_2^{eff}$.

$^{37}$Cl relaxation measurements were also made in every case and reflect the same relative differences between the samples. An important aspect to note is the comparison of the $T_1$ values between $^{35}$Cl and $^{37}$Cl (Table 2). In every case, the $T_1(^{37}Cl) > T_1(^{35}Cl)$. The dramatic decrease in $T_1(^{37}Cl)$ between **$LaCl_3$** and the other samples, as well as the $T_1(^{37}Cl)$'s of the paramagnetic samples correlating with their magnetic moments (Fig. 3b), suggests the same PRE effects as $^{35}$Cl. Similar to $^{35}$Cl, the $T_2^{eff}(^{37}Cl)$ values match the $\mu_{eff}$ trends (Fig. 3b). As with $T_1$ measurements it is also observed that $T_2^{eff}(^{37}Cl) > T_2^{eff}(^{35}Cl)$. The differences between $^{37}$Cl and $^{35}$Cl are the gyromagnetic ratios, $\gamma$, and the measured $C_Q$'s. The former could cause an additional PRE contribution for each spin isotope (*i.e.*, a PRE originating from scaling $\gamma$ rather than $\mu_{eff}$ as discussed above). Whereas the latter could indicate the influence of a quadrupolar relaxation mechanism in these spin systems. This facet is clear in the case of diamagnetic **$LaCl_3$** where the $^{37}$Cl relaxation times are longer in the absence of any PRE. Therefore, both the PRE and quadrupolar relaxation mechanisms are likely simultaneously contributing to the total rate of relaxation in these spin systems.

### 3.4. Density functional theory

DFT calculations are first used to unravel the various contributions to the observed $^{35/37}$Cl NMR spectra. In all cases, reasonable agreement to the experimentally observed EFG tensor parameters are obtained with the DFT+$U$ calculations with close agreement for **$LaCl_3$**, **$NdCl_3$** and **$UCl_4$** (Table 1). Agreement with the experimental tensor values for **$UCl_3$** can be obtained by a +$U$ correction to the 6d-orbitals in lieu of the 5f-orbitals but at the consequence of the incorrect electronic structures (see discussion in the SI). Therefore, +$U$ corrections can only be applied to the 5f-orbitals for **$UCl_3$**, which yields a slightly higher deviation from the experimental values.

We also probe the effects of the electron hyperfine field from the paramagnetic metals on the $^{35/37}$Cl SA using experimental and calculated results. The paramagnetic shielding tensor, $\boldsymbol{\sigma}_S$, is obtained from the calculated hyperfine tensor, **A**, and the g tensor, **g**, with the following relationship,[115]

$$\boldsymbol{\sigma}_S = \frac{\mu_B S(S+1)}{3\hbar\gamma_N k_B(T-\Theta)}\mathbf{g}\cdot\mathbf{A} \quad (1)$$

where, $\mu_B$ is the Bohr magneton, $S$ is the electronic spin quantum number, $\gamma_N$ is the gyromagnetic ratio of the observe nucleus ($^{35/37}$Cl), $k_B$ is the Boltzmann constant, $T$ is the temperature in K, and $\Theta$ is the Curie–Weiss constant. The inclusion of the Weiss constant in eqn (1) compensates for the bulk magnetic susceptibility effects. This equation is used to determine the full SA tensor by substituting the associated principal components of the **A** and **g** tensors following the procedure outlined by Pigliapochi *et al.*[115] Here we use the previously reported **g**-tensors for **$UCl_3$**,[116] the tensor for $Nd^{3+}$ in **$LaCl_3$**,[117] and $U^{4+}$ in $CaF_2$.[118]

The calculated SA results for **$NdCl_3$**, **$UCl_3$** and **$UCl_4$** are given in Table 1. With the overwhelming influence of **A** and the lack of experimental values, diamagnetic contributions to the SA are not reported, which yields no SA for the pure diamagnetic **$LaCl_3$** case. For **$NdCl_3$**, the DFT calculations substantially overestimate the $\delta_{iso}$ using the literature **g** values. However, the results for **$UCl_3$** and **$UCl_4$** show relatively higher agreement to the measured $^{35/37}$Cl $\delta_{iso}$'s. The calculated **A** contribution to the span, $\Omega$, is in good agreement for **$UCl_3$**, and **$NdCl_3$**, and underestimated for **$UCl_4$**. Investigating the relative contributions to the SA (Table S6) reveal that the contact shift contributions substantially contribute to both the isotropic and anisotropic portion of the SA with the sign and magnitude of the **g**-tensor having the largest impact on the anisotropy.

These calculations also do not explicitly model the effects of thermally accessible excited electronic states that arise from

zero-field splitting (ZFS) or crystal-field splitting (CFS) present in f-block metals. ZFS is known to impact chemical shifts in solution-state NMR of heavy element containing compounds and has been extensively described theoretically.[119,120] Promising efforts have been made to incorporate these effects into solid-state NMR paramagnetic chemical shift calculations.[121] However, the contributions of electron–electron repulsion, spin–orbit coupling, and CFS have been shown to contribute nearly equally to the magnetic properties of the actinide elements and can only be disentangled through extensive computational efforts.[122] Although application of these methods to actinide and lanthanide-containing materials could improve the inaccuracies present in the current study, such developments remain a challenge.

The DFT results can be further used to investigate the differences in the M–Cl bonds in these materials. In all the samples studied, the single Cl site adopts a bridging environment between two metal atoms. In the trichloride compounds, the three bridging M–Cl distances differ by at most 0.3% for **$NdCl_3$**. However, in **$UCl_4$** the two bridging U–Cl bonds can be characterized as a short and a long bond with lengths of 2.64 Å and 2.89 Å, respectively. The differences in these bonding environments are investigated using the results from the LOBSTER analysis.[96–98] This analysis provides measurements of bond covalency by calculating the overlap in the orbital energies and provides the simple numerical values in the form of the COHP, and a unitless parameter denoted the COBI which is a unitless parameter scaled from 0 to 1 where 0 is a fully ionic bonding interaction and 1 is completely covalent. This program was also recently updated to calculate local molecular orbitals (LMO) from periodic DFT calculations, which they denote as RLMO.[98] Both **$UCl_3$** bonds and the longer **$UCl_4$** bonds have similar COBI values of 0.18 and 0.21, respectively which indicate a similar ionicity of these bonds. The COBI value of 0.38 for the shorter **$UCl_4$** bond indicates a slight increase in the covalency of this bond relative to the longer bonds. These differ slightly from the bond-weighted averages (ICHOP and ICOBI) in Table 1. This increased covalency results from the energy overlap between the Cl 3p and U 5f orbitals as revealed in the calculated density of states (DOS, Fig. S16).

Investigation of the RLMO for the Cl atom reveal a potential source of the increased covalency in **$UCl_4$**. Looking at the RLMOs corresponding to one of the Cl π lone pair orbitals for these two compounds (Fig. 4) indicates that the electron density for this orbital is highly localized close to the Cl center in **$UCl_3$** whereas in **$UCl_4$** the density extends slightly along the longer U–Cl bond. Similar results have been observed in calculations of actinide hexachloride salts and have been invoked to explain relative covalency differences in this series.[6] Further, in **$UCl_3$** $V_{zz}$ is negative and points directly at the σ lone-pair orbital (Fig. 4b), which is characteristic of a more ionic bond.[123] Contrastingly, $V_{zz}$ for the **$UCl_4$** EFG tensor is positive and lies nearly parallel to the vector between the two U metal centers (Fig. 4d), which could suggest potential contributions from dative bonding between the U and Cl like that observed for previously in heavy transition-metal chlorides.[33,34] The increased covalency in

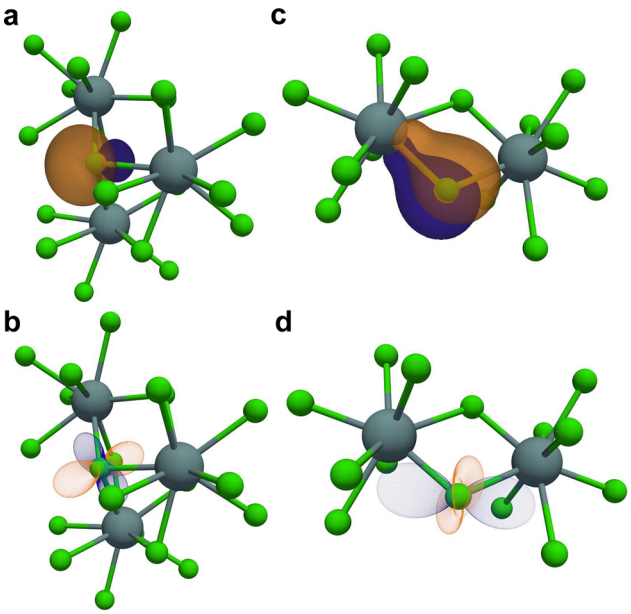


Fig. 4 Graphical representations of the RLMO for (a) the $\sigma$ lone pair for **$UCl_3$** and (b) the ovaloid representation of the $^{35/37}$Cl EFG tensor at the corresponding Cl atom. (c) The RLMO for the π lone pair for **$UCl_4$** and (d) the $^{35/37}$Cl EFG tensor. Orange and blue isosurfaces indicate negative and positive charge densities, respectively.

**$UCl_4$** likely explains the large $\Omega$, as there will be a larger $\mathbf{A}_D$ contribution when the U f electrons are closer to the $^{35/37}$Cl spins. It is unclear why the DFT calculations of **A** do not reflect this increase, but it could be linked to absence of spin–orbit paramagnetic effects and ZFS not being adequately captured. However, these results must be interpreted with care since VASP and LOBSTER project onto the electron density predicted onto *lm*-decomposed orbitals and although spin–orbit coupling is included in calculations, some differences with respect to the full Dirac equation could change the electron density, including the $5p_{1/2}$ and $6p_{1/2}$ states that overlap significantly with the nucleus.[124–126] More work incorporating relativistic calculations based on the Dirac equation are likely required to fully understand these bonding interactions. Taken together, the results from the RLMO and DFT analysis suggest the increase in bond covalency for the U–Cl bond in **$UCl_4$** is responsible for both the increase in the $^{35/37}$Cl $C_Q$ and the dipolar contributions to the SA.

## 4. Conclusions

$^{35/37}$Cl SSNMR of lanthanide and actinide chloride salts measured under static conditions offers a simple and sensitive measure of the paramagnetic SA effects without needing isotopic enrichment or specialized equipment. Some of the largest $^{35/37}$Cl SA parameters are reported for these materials, which is onset from the paramagnetic shielding resulting from hyperfine fields in uranium. The effects of bulk magnetic susceptibility likely introduce less inhomogeneous broadening than what can be resolved experimentally. The interplay of EFG and SA tensors offers a high-level of structural detail in a single

experiment and offers an extremely unique spectral fingerprint of the analyte, which will be beneficial for future product characterization and identification. These measurements benchmark $^{35/37}$Cl shift ranges for $U^{3+}$- and $U^{4+}$-containing chloride compounds, which will further aid in future product characterization. All materials studied herein feature one chlorine site, but compounds or mixtures with multiple sites can still be resolved under static conditions.[107,127] Static measurements at a single field alleviate safety concerns when measuring radioactive actinide materials. Measurements presented herein are relatively quick and simple to execute (*i.e.*, $<4$ hours for the longest $^{35}$Cl measurement) and can be improved upon with static probes and larger coils, which may enable more advanced $^{35}$Cl–$^{37}$Cl correlation experiments.[128] $^{37}$Cl measurements are approximately three-times slower but are ultimately not necessary to perform depending on the application. The size of the SA contribution hinders the CPMG-type acquisition presented herein, since the PRE shortens the $T_2$; however, later actinides such as Pu and Am should exhibit less paramagnetic susceptibility than $U^{3+}$, which would make the respective measurements of **$PuCl_3$** and $AmCl_3$ easier than **$UCl_3$**.

DFT calculations using Hubbard+*U* corrections can help constrain the EFG and **A** tensor parameters and can enable easier independent identification of SA tensor parameters. Furthermore, these calculations provide an insight to the relative contributions of ionic and covalent bonding in the U–Cl systems, where experiments and calculations indicate a higher degree of bond covalency in **$UCl_4$** than **$UCl_3$**. Our strategies for fast and reliable static measurements of actinide chloride salts will pave the way for high-throughput analysis useful to the molten salt reactor community and to researchers pursuing synthetic and fundamental advancements in actinide chemistry.

## Conflicts of interest

There are no conflicts to declare.

## Data availability

All simulation input files, processing functions and scripts, and NMR datasets are available from the authors by request.

Supplementary information (SI): additional simulations, experiments, and experimental details. See DOI: https://doi.org/10.1039/d5cp03944d.

## Acknowledgements

Research presented in this report was supported by the Laboratory Directed Research and Development program of Los Alamos National Laboratory under project number 20230728DI. Los Alamos National Laboratory is operated by Triad National Security, LLC, for the National Nuclear Security Administration of US Department of Energy (contract no. 89233218CNA000001). The authors thank Professor Rob Schurko for helpful discussions.

## References

1 T. V. Fetrow, J. P. Grabow, J. Leddy and S. R. Daly, *Inorg. Chem.*, 2021, **60**, 7593–7601.
2 D. Patel, A. J. Wooles, E. Hashem, H. Omorodion, R. J. Baker and S. T. Liddle, *New J. Chem.*, 2015, **39**, 7559–7562.
3 J. L. Kiplinger, D. E. Morris, B. L. Scott and C. J. Burns, *Organometallics*, 2002, **21**, 5978–5982.
4 D.-C. Sergentu and J. Autschbach, *Chem. Sci.*, 2022, **13**, 3194–3207.
5 S. A. Kozimor, P. Yang, E. R. Batista, K. S. Boland, C. J. Burns, D. L. Clark, S. D. Conradson, R. L. Martin, M. P. Wilkerson and L. E. Wolfsberg, *J. Am. Chem. Soc.*, 2009, **131**, 12125–12136.
6 C. L. Silva, L. Amidani, M. Retegan, S. Weiss, E. F. Bazarkina, T. Graubner, F. Kraus and K. O. Kvashnina, *Nat. Commun.*, 2024, **15**, 6861.
7 J. N. Cross, J. Su, E. R. Batista, S. K. Cary, W. J. Evans, S. A. Kozimor, V. Mocko, B. L. Scott, B. W. Stein and C. J. Windorff, *et al.*, *J. Am. Chem. Soc.*, 2017, **139**, 8667–8677.
8 S. G. Minasian, J. M. Keith, E. R. Batista, K. S. Boland, D. L. Clark, S. D. Conradson, S. A. Kozimor, R. L. Martin, D. E. Schwarz and D. K. Shuh, *et al.*, *J. Am. Chem. Soc.*, 2012, **134**, 5586–5597.
9 L. Peng; R. J. Clément; M. Lin and Y. Yang, CHAPTER 1: NMR Principles of Paramagnetic Materials. *In New Developments in NMR*, The Royal Society of Chemistry, 2021, Vol. 2021, pp. 3–70.
10 N. F. Ramsey, *Phys. Rev.*, 1950, **78**, 695–699.
11 N. F. Ramsey, *Phys. Rev.*, 1950, **78**, 699–703.
12 N. F. Ramsey, *Phys. Rev.*, 1950, **77**, 567.
13 N. F. Ramsey, *Phys. Rev.*, 1951, **83**, 540–541.
14 N. F. Ramsey, *Phys. Rev.*, 1952, **86**, 243–246.
15 J. P. Carvalho, W. Papawassiliou and A. J. Pell, *J. Magn. Reson.*, 2022, **340**, 107235.
16 A. J. Pell, G. Pintacuda and C. P. Grey, *Prog. Nucl. Magn. Reson. Spectrosc.*, 2019, **111**, 1–271.
17 H. Yasuoka, G. Koutroulakis, H. Chudo, S. Richmond, D. K. Veirs, A. I. Smith, E. D. Bauer, J. D. Thompson, G. D. Jarvinen and D. L. Clark, *Science*, 2012, **336**, 901–904.
18 A. P. Dioguardi, H. Yasuoka, S. M. Thomas, H. Sakai, S. K. Cary, S. A. Kozimor, T. E. Albrecht-Schmitt, H. C. Choi, J.-X. Zhu and J. D. Thompson, *et al.*, *Phys. Rev. B: Condens. Matter Mater. Phys.*, 2019, **99**, 035104.
19 N. J. Curro, T. Caldwell, E. D. Bauer, L. A. Morales, M. J. Graf, Y. Bang, A. V. Balatsky, J. D. Thompson and J. L. Sarrao, *Phys. B*, 2006, **378–380**, 915–919.
20 K. Ikushima, S. Tsutsui, Y. Haga, H. Yasuoka, R. E. Walstedt, N. M. Masaki, A. Nakamura, S. Nasu and Y. Ōnuki, *Phys. Rev. B*, 2001, **63**, 104404.
21 R. E. Walstedt, Y. Tokunaga, H. Kato, H. Sakai, T. Fujimoto, S. Kambe and H. Yasuoka, *J. Phys. Soc. Jpn.*, 2006, **75**, 77–81.

22 K. D. Morrison, M. Zavarin, A. B. Kersting, J. D. Begg, H. E. Mason, E. Balboni and Y. Jiao, *Environ. Sci. Technol.*, 2021, **55**, 1626–1636.
23 E. C. Uribe, H. E. Mason, J. A. Shusterman, A. Bruchet and H. Nitsche, *Dalton Trans.*, 2016, **45**, 10447–10458.
24 E. C. Uribe, H. E. Mason, J. A. Shusterman and W. W. Lukens, *Dalton Trans.*, 2017, **46**, 5441–5456.
25 Y. Tokunaga, Y. Homma, S. Kambe, D. Aoki, H. Sakai, E. Yamamoto, A. Nakamura, Y. Shiokawa, R. E. Walstedt and H. Yasuoka, *Phys. Rev. Lett.*, 2005, **94**, 137209.
26 Y. Tokunaga, D. Aoki, Y. Homma, S. Kambe, H. Sakai, S. Ikeda, T. Fujimoto, R. E. Walstedt, H. Yasuoka and E. Yamamoto, *et al.*, *Phys. Rev. Lett.*, 2006, **97**, 17–20.
27 Y. Tokunaga, Y. Homma, S. Kambe, D. Aoki, H. Sakai, E. Yamamoto, A. Nakamura, Y. Shiokawa, R. E. Walstedt and H. Yasuoka, *Phys. B*, 2006, **378–380**, 929–930.
28 Y. Tokunaga, D. Aoki, Y. Homma, S. Kambe, H. Sakai, S. Ikeda, T. Fujimoto, R. E. Walstedt, H. Yasuoka and Y. Shiokawa, *et al.*, *J. Magn. Magn. Mater.*, 2007, **310**, 735–737.
29 Y. Tokunaga, T. Nishi, S. Kambe, M. Nakada, Y. Homma, H. Sakai and H. Chudo, *J. Phys. Soc. Jpn.*, 2011, **80**, 2010–2012.
30 L. Martel, N. Magnani, J.-F. Vigier, J. Boshoven, C. Selfslag, I. Farnan, J.-C. Griveau, J. Somers and T. Fanghänel, *Inorg. Chem.*, 2014, **53**, 6928–6933.
31 I. Farnan, H. Cho, W. J. Weber, R. D. Scheele, N. R. Johnson and A. E. Kozelisky, *Rev. Sci. Instrum.*, 2004, **75**, 5232–5236.
32 D. L. Bryce and G. D. Sward, *Magn. Reson. Chem.*, 2006, **44**, 409–450.
33 C. M. Widdifield; R. P. Chapman and D. L. Bryce, Chapter 5 Chlorine, Bromine, and Iodine Solid-State NMR Spectroscopy. *In Annual Reports on NMR Spectroscopy*, Elsevier Ltd., 2009, Vol. 66, pp. 195–326.
34 P. M. J. Szell and D. L. Bryce, Recent Advances in Chlorine, Bromine, and Iodine Solid-State NMR Spectroscopy, *In Annual Reports on NMR Spectroscopy*, Elsevier Ltd., 2015, Vol. 84, pp. 115–162.
35 P. M. J. Szell and D. L. Bryce, *Concepts Magn. Reson., Part A*, 2016, **45A**, e21412.
36 L. A. O'Dell and R. W. Schurko, *Chem. Phys. Lett.*, 2008, **464**, 97–102.
37 L. A. O'Dell, A. J. Rossini and R. W. Schurko, *Chem. Phys. Lett.*, 2009, **468**, 330–335.
38 A. J. Rossini, H. Hamaed and R. W. Schurko, *J. Magn. Reson.*, 2010, **206**, 32–40.
39 D. A. Hirsh, A. J. Rossini, L. Emsley and R. W. Schurko, *Phys. Chem. Chem. Phys.*, 2016, **18**, 25893–25904.
40 J. Koppe and M. R. Hansen, *J. Phys. Chem. A*, 2020, **124**, 4314–4321.
41 I. Hung and Z. Gan, *J. Magn. Reson.*, 2010, **204**, 256–265.
42 M. J. Jaroszewicz, A. R. Altenhof, R. W. Schurko and L. Frydman, *J. Am. Chem. Soc.*, 2021, **143**, 19778–19784.
43 T. Wolf, A. Eden-Kossoy and L. Frydman, *Solid State Nucl. Magn. Reson.*, 2023, 101862.
44 J. J. Kimball, A. R. Altenhof, M. J. Jaroszewicz and R. W. Schurko, *J. Phys. Chem. A*, 2023, **127**, 9621–9634.
45 A. Venkatesh, M. P. Hanrahan and A. J. Rossini, *Solid State Nucl. Magn. Reson.*, 2017, **84**, 171–181.
46 A. V. Wijesekara, A. Venkatesh, B. J. Lampkin, B. VanVeller, J. W. Lubach, K. Nagapudi, I. Hung, P. L. Gor'kov, Z. Gan and A. J. Rossini, *Chem. – Eur. J.*, 2020, **26**, 7881–7888.
47 I. Hung and Z. Gan, *J. Phys. Chem. Lett.*, 2020, **11**, 4734–4740.
48 R. Bayzou, J. Trébosc, I. Hung, Z. Gan, O. Lafon and J.-P. Amoureux, *J. Chem. Phys.*, 2022, **156**, 064202.
49 I. Hung and Z. Gan, *J. Magn. Reson.*, 2023, **350**, 107423.
50 D. L. Bryce, Solid-state NMR of quadrupolar nuclei: Selected new methods and applications. *In Annual Reports on NMR Spectroscopy*, Elsevier Ltd., 2022, pp. 1–46.
51 H. Rinneberg, H. Haas and H. Hartmann, *J. Chem. Phys.*, 1969, **50**, 3064–3071.
52 H. Rinneberg and H. Hartmann, *J. Chem. Phys.*, 1970, **52**, 5814–5820.
53 A. Narath, *Phys. Rev.*, 1965, **140**, A552–A568.
54 W. J. O'Sullivan, W. W. Simmons and W. A. Robinson, *Phys. Rev.*, 1965, **140**, A1759–A1771.
55 W. H. Jones and S. L. Segel, *Phys. Rev. Lett.*, 1964, **13**, 528–530.
56 F. Engelke, D. Michel, W. Windsch, P. Sarv and E. Lippmaa, *Ferroelectrics*, 1990, **108**, 337–340.
57 H. Trill, H. Eckert and V. I. Srdanov, *Phys. Rev. B: Condens. Matter Mater. Phys.*, 2005, **71**, 014412.
58 D. Michel, U. Hacker, T. Erge and J. Petersson, *Phys. Status Solidi*, 1994, **185**, 257–264.
59 L. Bauder and G. Wu, *Magn. Reson. Chem.*, 2024, **62**, 145–155.
60 S. Park, E. D. Walter, C. Z. Soderquist, S. I. Sinkov and H. Cho, *J. Phys. Chem. A*, 2023, 8347–8353.
61 S. Park, R. G. Surbella, S. I. Sinkov, A. B. Philips, J. Autschbach and H. Cho, *Chem. Phys.*, 2023, **576**, 112094.
62 S. Antonijevic and S. Wimperis, *J. Chem. Phys.*, 2005, **122**, 044312.
63 S. Antonijevic and S. Wimperis, *J. Magn. Reson.*, 2003, **164**, 343–350.
64 T. Iijima and K. Nishimura, *Chem. Phys. Lett.*, 2011, **514**, 181–186.
65 T. Iijima, T. Shimizu and K. Nishimura, *J. Magn. Reson.*, 2015, **251**, 57–64.
66 M. Mizuno, N. Itakura and K. Endo, *Chem. Phys. Lett.*, 2005, **416**, 358–363.
67 T. Iijima, S. Ohki and M. Tansho, *Solid State Nucl. Magn. Reson.*, 2021, **112**, 101709.
68 R. Aleksis, J. P. Carvalho, A. Jaworski and A. J. Pell, *Solid State Nucl. Magn. Reson.*, 2019, 51–62.
69 R. Aleksis and A. J. Pell, *J. Chem. Phys.*, 2021, **155**, 094202.
70 J. T. Ash, N. M. Trease and P. J. Grandinetti, *J. Am. Chem. Soc.*, 2008, **130**, 10858–10859.
71 J. P. Carvalho, A. Jaworski, M. J. Brady and A. J. Pell, *Magn. Reson. Chem.*, 2020, **58**, 1055–1070.
72 D. L. Bryce, Tensor Interplay, *In Encyclopedia of Magnetic Resonance*, 2009.

73 F. A. Perras, C. M. Widdifield and D. L. Bryce, *Solid State Nucl. Magn. Reson.*, 2012, **45–46**, 36–44.
74 D. L. Bryce, G. D. Sward and S. Adiga, *J. Am. Chem. Soc.*, 2006, **128**, 2121–2134.
75 I. Hung, A. R. Altenhof, R. W. Schurko, D. L. Bryce, O. H. Han and Z. Gan, *Magn. Reson. Chem.*, 2021, **59**, 951–960.
76 K. A. Erickson, S. S. Parker and M. J. Monreal, *Chem.: Methods*, 2024, **4**, 3–5.
77 J. A. Hermann; J. F. Suttle and H. R. Hoekstra, Uranium(IV) Chloride, *In Inorganic Syntheses*, John Wiley & Sons Ltd, Hoboken, New Jersey, 1957, pp. 143–145.
78 L. A. O'Dell, *Solid State Nucl. Magn. Reson.*, 2013, **55–56**, 28–41.
79 R. W. Schurko, Acquisition of Wideline Solid-State NMR Spectra of Quadrupolar Nuclei, *In Encyclopedia of Magnetic Resonance*, John Wiley & Sons, Ltd, Chichester, UK, 2011, pp. 77–93.
80 R. W. Schurko, *Acc. Chem. Res.*, 2013, **46**, 1985–1995.
81 X. Guan and R. E. Stark, *Solid State Nucl. Magn. Reson.*, 2010, **38**, 74–76.
82 A. R. Altenhof, M. J. Jaroszewicz, K. J. Harris and R. W. Schurko, *J. Chem. Phys.*, 2021, **154**, 034202.
83 A. R. Altenhof, H. Mason and R. W. Schurko, *J. Magn. Reson.*, 2023, **346**, 107320.
84 J. J. Helmus and C. P. Jaroniec, *J. Biomol. NMR*, 2013, **55**, 355–367.
85 M. J. Jaroszewicz, A. R. Altenhof, R. W. Schurko and L. Frydman, *J. Magn. Reson.*, 2023, **354**, 107528.
86 S. G. J. van Meerten, W. M. J. Franssen and A. P. M. Kentgens, *J. Magn. Reson.*, 2019, **301**, 56–66.
87 M. Bak, J. T. Rasmussen and N. C. Nielsen, *J. Magn. Reson.*, 2011, **213**, 366–400.
88 Z. Tošner, R. Andersen, B. Stevensson, M. Edén, N. C. Nielsen and T. Vosegaard, *J. Magn. Reson.*, 2014, **246**, 79–93.
89 G. Kresse and J. Hafner, *Phys. Rev. B: Condens. Matter Mater. Phys.*, 1993, **47**, 558–561.
90 G. Kresse and J. Hafner, *J. Phys.: Condens. Matter*, 1994, **6**, 8245–8257.
91 G. Kresse and J. Furthmüller, *Phys. Rev. B: Condens. Matter Mater. Phys.*, 1996, **54**, 11169–11186.
92 G. Kresse and J. Furthmüller, *Comput. Mater. Sci.*, 1996, **6**, 15–50.
93 J. P. Perdew, A. Ruzsinszky, G. I. Csonka, O. A. Vydrov, G. E. Scuseria, L. A. Constantin, X. Zhou and K. Burke, *Phys. Rev. Lett.*, 2008, **100**, 136406.
94 S. L. Dudarev, G. A. Botton, S. Y. Savrasov, C. J. Humphreys and A. P. Sutton, *Phys. Rev. B: Condens. Matter Mater. Phys.*, 1998, **57**, 1505–1509.
95 J. Kim, D. S. Middlemiss, N. A. Chernova, B. Y. X. Zhu, C. Masquelier and C. P. Grey, *J. Am. Chem. Soc.*, 2010, **132**, 16825–16840.
96 P. C. Müller, C. Ertural, J. Hempelmann and R. Dronskowski, *J. Phys. Chem. C*, 2021, **125**, 7959–7970.
97 R. Nelson, C. Ertural, J. George, V. L. Deringer, G. Hautier and R. Dronskowski, *J. Comput. Chem.*, 2020, **41**, 1931–1940.
98 M. Pauls, D. Schnieders and R. Dronskowski, *J. Phys. Chem. A*, 2023, **127**, 6541–6551.
99 B. Morosin, *J. Chem. Phys.*, 1968, **49**, 3007–3012.
100 J. C. Taylor and P. W. Wilson, *Acta Crystallogr., Sect. B: Struct. Crystallogr. Cryst. Chem.*, 1974, **30**, 2803–2805.
101 J. C. Taylor and P. W. Wilson, *Acta Crystallogr., Sect. B: Struct. Crystallogr. Cryst. Chem.*, 1973, **29**, 1942–1944.
102 C. A. O'Keefe, K. E. Johnston, K. Sutter, J. Autschbach, L. Delevoye, N. Popo, M. Taou, K. Oudatchin and R. W. Schurko, *Inorg. Chem.*, 2014, **53**, 9581–9597.
103 J. H. Kristensen, G. L. Hoatson and R. L. Vold, *Solid State Nucl. Magn. Reson.*, 1998, **13**, 1–37.
104 R. L. Vold and G. L. Hoatson, *J. Magn. Reson.*, 2009, **198**, 57–72.
105 C. S. Vojvodin, S. T. Holmes, L. K. Watanabe, J. M. Rawson and R. W. Schurko, *CrystEngComm*, 2022, **24**, 2626–2641.
106 D. R. Kindra and W. J. Evans, *Chem. Rev.*, 2014, **114**, 8865–8882.
107 M. J. Jaroszewicz, L. Frydman and R. W. Schurko, *J. Phys. Chem. A*, 2017, **121**, 51–65.
108 J. S. Frye, *Concepts Magn. Reson.*, 1989, **1**, 27–33.
109 E. D. Becker, J. A. Ferretti, R. K. Gupta and G. H. Weiss, *J. Magn. Reson.*, 1980, **37**, 381–394.
110 E. D. Ostroff and J. S. Waugh, *Phys. Rev. Lett.*, 1966, **16**, 1097–1098.
111 J. S. Waugh, C. H. Wang, L. M. Huber and R. L. Vold, *J. Chem. Phys.*, 1968, **48**, 662–670.
112 M. Hürlimann and D. Griffin, *J. Magn. Reson.*, 2000, **143**, 120–135.
113 S. L. Veinberg, A. W. Lindquist, M. J. Jaroszewicz and R. W. Schurko, *Solid State Nucl. Magn. Reson.*, 2016, 1–14.
114 A. R. Altenhof, Z. Gan and R. W. Schurko, *J. Magn. Reson.*, 2022, 337.
115 R. Pigliapochi, A. J. Pell, I. D. Seymour, C. P. Grey, D. Ceresoli and M. Kaupp, *Phys. Rev. B*, 2017, **95**, 054412.
116 C. A. Hutchison, P. M. Llewellyn, E. Wong and P. Dorain, *Phys. Rev.*, 1956, **102**, 292.
117 J. D. Riley, J. M. Baker and R. J. Birgeneau, *Proc. R. Soc. London. A. Math. Phys. Sci.*, 1970, **320**, 369–395.
118 G. Garton, M. T. Hutchings, R. Shore and W. P. Wolf, *J. Chem. Phys.*, 1964, **41**, 1970–1974.
119 V. Lupei and C. Stoicescu, *J. Phys. C:Solid State Phys.*, 1979, **12**, 4585–4590.
120 F. Gendron and J. Autschbach, *J. Chem. Theory Comput.*, 2016, **12**, 5309–5321.
121 A. Mondal and M. Kaupp, *J. Phys. Chem. C*, 2019, **123**, 8387–8405.
122 K. Georgiadis, Computational Modelling of Molecular Nanomagnets, ed G. Rajaraman, *Challenges and Advances in Computational Chemistry and Physics*, Springer International Publishing, Cham, 2023, Vol. 34.
123 J. Autschbach, S. Zheng and R. W. Schurko, *Concepts Magn. Reson., Part A*, 2010, **36A**, 84–126.
124 D. A. Rehn, J. M. Wills, T. E. Battelle and A. E. Mattsson, *Phys. Rev. B*, 2020, **101**, 085114.
125 J. Autschbach, *Relativistic Effects on NMR Parameters. In Science and Technology of Atomic, Molecular, Condensed*

*Matter and Biological Systems*, Elsevier Inc., 2013, Vol. 3, pp. 69–117.
126 J. Vicha, J. Novotný, S. Komorovsky, M. Straka, M. Kaupp and R. Marek, *Chem. Rev.*, 2020, **120**, 7065–7103.
127 A. R. Altenhof, M. J. Jaroszewicz, L. Frydman and R. Schurko, *Phys. Chem. Chem. Phys.*, 2022, 22792–22805.
128 T. Wolf, M. J. Jaroszewicz and L. Frydman, *J. Phys. Chem. C*, 2022, **126**, 9386–9395.
129 M. Mehring, *Principles of High Resolution NMR in Solids*, Springer Berlin Heidelberg, Berlin, Heidelberg, 1983.
130 S. Adiga, D. Aebi and D. L. Bryce, *Can. J. Chem.*, 2007, **85**, 496–505.

 